Giant switchable photovoltaic effect in organometal trihalide perovskite devices

Zhengguo Xiao[1,2†], Yongbo Yuan[1,2†], Yuchuan Shao[1,2†], Qi Wang[1,2], Qingfeng Dong[1,2], Cheng Bi[1,2], Pankaj Sharma[2,3], Alexei Gruverman[2,3] and Jinsong Huang[1,2]*

Organolead trihalide perovskite (OTP) materials are emerging as naturally abundant materials for low-cost, solution-processed and highly efficient solar cells[1-9]. Here, we show that, in OTP-based photovoltaic devices with vertical and lateral cell configurations, the photocurrent direction can be switched repeatedly by applying a small electric field of <1 V μm⁻¹. The switchable photocurrent, generally observed in devices based on ferroelectric materials, reached 20.1 mA cm⁻² under one sun illumination in OTP devices with a vertical architecture, which is four orders of magnitude larger than that measured in other ferroelectric photovoltaic devices[10,11]. This field-switchable photovoltaic effect can be explained by the formation of reversible p–i–n structures induced by ion drift in the perovskite layer. The demonstration of switchable OTP photovoltaics and electric-field-manipulated doping paves the way for innovative solar cell designs and for the exploitation of OTP materials in electrically and optically readable memristors and circuits.

The vertical structure device has a layered structure of indium tin oxide (ITO)/poly(3,4-ethylenedioxythiophene):poly(4-styrenesulphonate) (PEDOT:PSS)/perovskite/Au, as shown in Fig. 1a, where the methylammonium lead iodide (MAPbI₃) perovskite layer was formed by the interdiffusion of lead iodide (PbI₂) and methylammonium halide (MAI) stacking layers[12]. The as-prepared devices with 300 nm thick perovskite films have a J_{SC} of 8.5 mA cm⁻² and V_{OC} of 0.18 V (Supplementary Fig. 1), despite the work functions of PEDOT:PSS and Au electrodes being almost the same. This might be due to the different interfacial electronic structures at the perovskite/PEDOT:PSS and perovskite/Au contacts. A large memristive effect from these devices was identified, both in the dark and under illumination, which showed a scanning-history-dependent current output (Supplementary Fig. 2). The diode direction can be switched during the scanning process in the dark, as shown in Fig. 1b. The on/off ratios of the dark current are >10³ and >10² at biases of −1.0 V and 0.7 V, respectively. The devices can also be poled by a constant bias pulse with a duration of 5–30 s (Supplementary Fig. 3a,b). The device with a perovskite layer thickness of 1,015 nm was switched by a small bias of 1.0 V (Supplementary Fig. 3c), which corresponds to a minimal poling electric field of <1 V μm⁻¹.

The switchable diode in the dark resulted in a giant switchable photovoltaic effect under illumination. In contrast to switchable photovoltaics using bismuth ferrite materials, with J_{SC} typically of the order of ~μA cm⁻² (refs 10,11), J_{SC} for the OTP devices switched between 18.6 and −20.1 mA cm⁻² (Fig. 1c) under one sun

illumination, which is comparable to that of optimized perovskite solar cells[1-5,13]. This indicates that most of the photogenerated excitons dissociated to free charges in the perovskite layer, even without an electron- or hole-accepting layer, and the free charges were efficiently collected by the electrodes regardless of the diode directions. The photocurrents showed a variety of hysteresis loops with changed scanning rates, whereas J_{SC} remained almost unchanged and V_{OC} was around 0.15 V lower at a lower scanning rate of 0.25 V s⁻¹, as shown in Supplementary Fig. 2b–d. The photocurrent direction after poling remained unchanged after storing the device for two months under ambient illumination in the glovebox (Supplementary Fig. 4). The value of V_{OC} was switched between 0.42 V and −0.73 V. There is a variation in J_{SC} and V_{OC} from different devices; some of them showed a larger V_{OC}, close to 0.9 V, but with a relatively smaller J_{SC} of 8 mA cm⁻² (Supplementary Fig. 5). The average V_{OC} and J_{SC} of the vertical structure devices were ±0.65 V and ±18.5 mA cm⁻², respectively (Supplementary Fig. 5). Positive poling (electric field pointing from PEDOT:PSS to Au) resulted in a positive V_{OC}. A typical device was switched more than 750 times with the V_{OC} in the first ten and last ten poling cycles shown in Fig. 1d. The photocurrent direction of the device can survive after 750 poling cycles. After positive poling, V_{OC} remained almost constant at 0.42 V, whereas after negative poling, V_{OC} showed switching fatigue from 0.73 V to 0.21 V. The switchable photovoltaic phenomenon was universally demonstrated using other OTP materials, such as CH₃NH₃PbI₃₋ₓClₓ, HC(NH₂)₂PbI₃ and CH₃NH₃PbBr₃ (Supplementary Fig. 6), and with many other top electrodes, including nickel, gallium and platinum (Supplementary Fig. 7), but not aluminium or silver, owing to the severe chemical reaction of perovskite with aluminium and silver.

We moved on to demonstrate the switchable photovoltaic effect in lateral structure devices because of the very low electric field of 1 V μm⁻¹ needed for poling and the absence of electrode selectivity shown in the vertical structure devices. Fig. 2a shows a schematic of a photovoltaic device with a lateral symmetric structure of Au/OTP/Au/OTP/..., where tens to hundreds of cells are connected in series. Fig. 2b shows the optical image of a Au electrode pattern fabricated by photolithography, where the electrode spacing is 8 μm. As shown in Fig. 2c, the non-poled device showed no photovoltaic effect with zero V_{OC} because of the symmetrical electrodes, whereas the poled single cell showed a V_{OC} of 0.48 V under 0.25 sun illumination after poling at 10 V for ~100 s. The photovoltaic direction after poling was consistent with that of the vertical structure devices. The photovoltaic direction was flipped by a reversed poling bias. In contrast to ferroelectric photovoltaics[14],
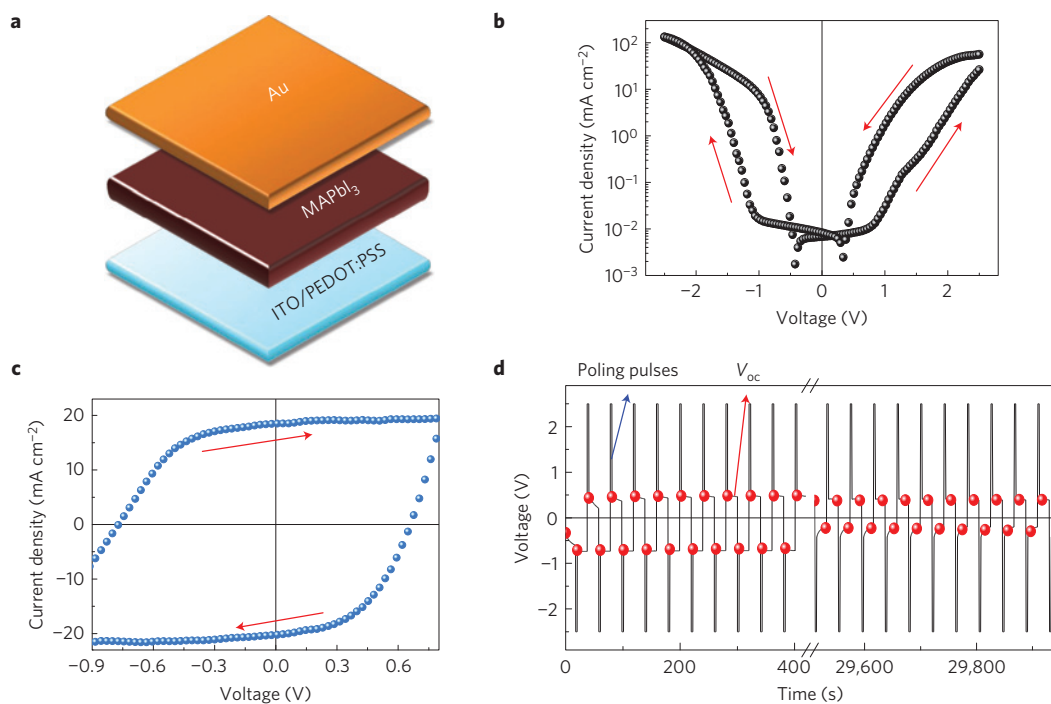
Figure 1 | Vertical structure photovoltaic devices and their switching behaviour. a, Schematic of the vertical structure device. **b,c**, Dark current (**b**) and photocurrent hysterisis curves (**c**) of the devices under continuous current sweeping at a rate of 0.14 V s^{-1} between −2.5 V and 2.5 V. The arrows in the figures show the scanning direction. **d**, Open circuit voltage of the device recorded after repeated poling by ±2.5 V bias for more than 750 cycles. Only the first ten and last ten cycles are shown. The red dots refer to V_{OC} of the device after positive and negative poling.
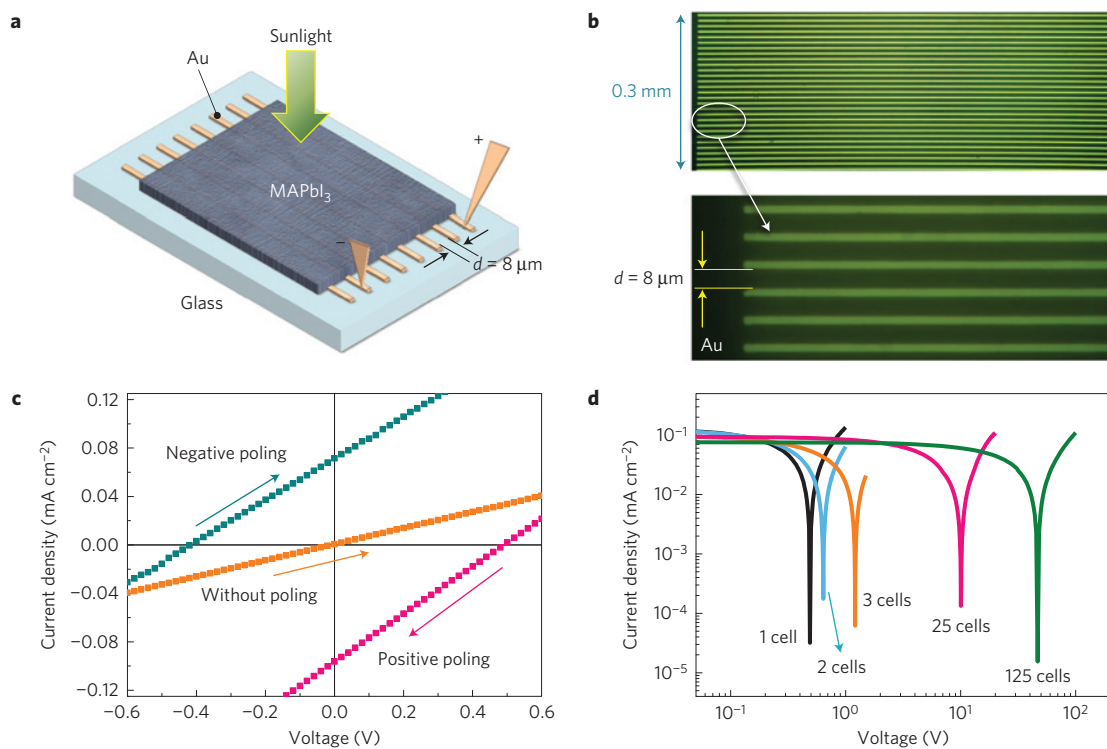

Figure 2 | Lateral structure photovoltaic devices and their switching behaviour. a, Schematic of the lateral structure devices. **b**, A Au stripe array under a microscope (reflective mode), where the electrode spacing, d, shown in the enlarged image below, is 8 μm. Lateral photovoltaic devices connected in series were fabricated by depositing uniform perovskite films (300 nm) on pre-formed Au stripe electrodes with spacings between 8 and 100 μm.
c, Photocurrents of the device before and after negative and positive poling for a single cell measured at a sweeping rate of 0.05 V s^{-1} under 0.25 sun illumination; the arrows in the figure indicate the scanning direction. **d**, Photocurrents of lateral photovoltaic devices connected in series measured at a sweeping rate of ∼0.05 V s^{-1} for each cell. The poling of the lateral photovoltaic devices was conducted either by poling each cell individually or by simply poling the whole area between the first and last electrodes.
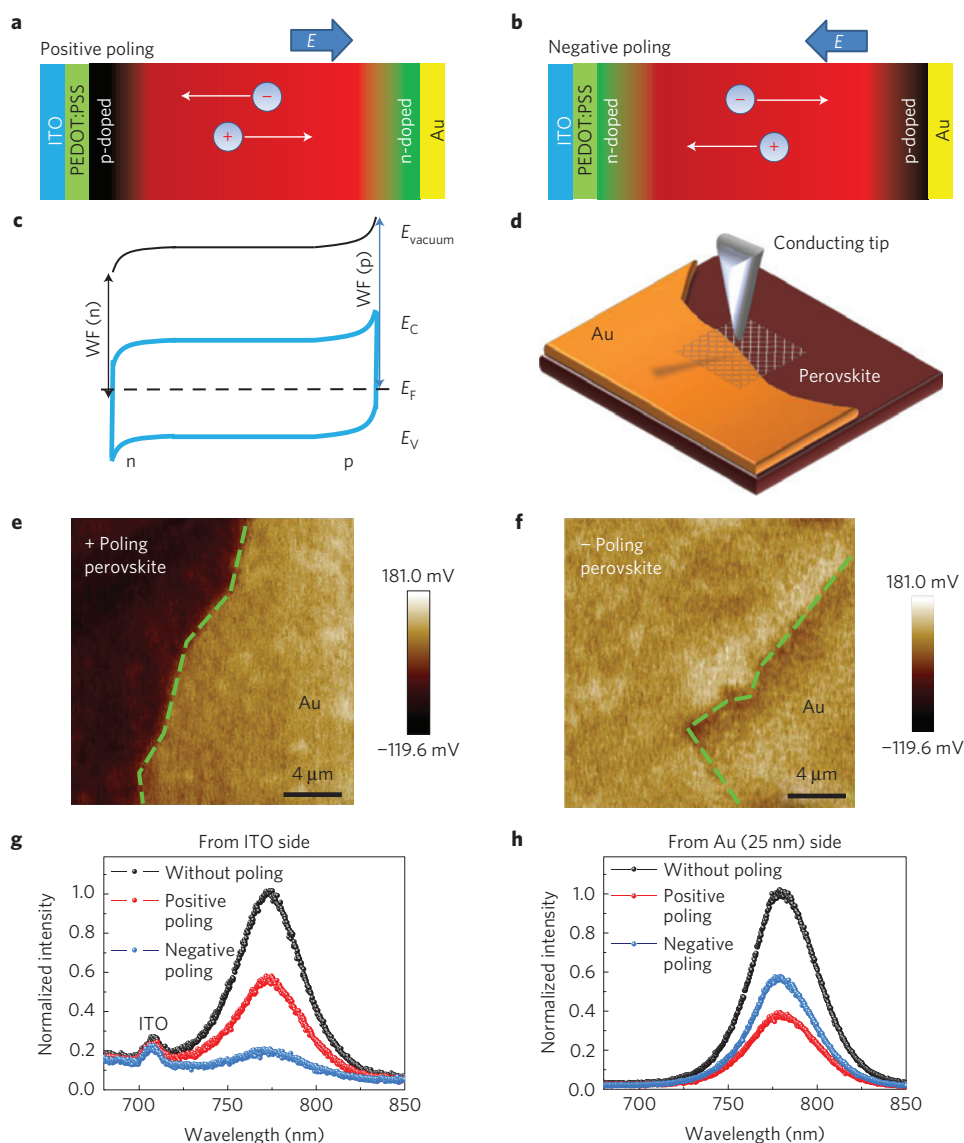
Figure 3 | Switchable photovoltaic model and mechanism study. a,b, Schematics of ion drift in perovskite during positive and negative poling, respectively, showing that accumulated ions in the perovskite near the electrodes induced p- and n-doping. **c,** Energy diagram of the p–i–n structure after poling. WF, workfunction. **d,** Schematic image of a device with part of the Au electrode peeled off. The scanned area is marked as a dashed rectangle. **e,f,** KPFM potential image of the perovskite/Au areas after positive and negative poling, respectively, of the perovskite layers (300 nm). **g,h,** Photoluminescence from the thin perovskite layers close to either a PEDOT:PSS electrode or a Au electrode. A thin gold electrode (25 nm) was used as the top electrode so the photoluminescence emission from the perovskites close to both electrodes can be measured. Blue light (405 nm) was used to excite only the 25 nm thick perovskite layer close to the electrodes (estimated by the extinction coefficient) of the 1,015 nm thick device. The photoluminescence measurement was conducted *in situ* during the poling process to exclude other factors affecting photoluminescence. The small extra peak at 710 nm in **g** is due to the ITO.

the V_{OC} of a single device after poling remains almost constant at around 0.50 V for a range of electrode spacings from 8 to 100 μm (Supplementary Fig. 9). The J_{SC} value of the device with an 8 μm electrode spacing is 0.1 mA cm^{-2}. The smaller J_{SC} in the lateral structure devices is due to the electrode spacing being much larger than the charge diffusion length in perovskite materials[15,16]. The statistics of the performance of the lateral structure devices is shown in Supplementary Fig. 8. The largest absolute V_{OC} and J_{SC} values reached 0.88 V and 0.11 mA cm^{-2}, and the average V_{OC} and J_{SC} values of the lateral structure devices were ±0.50 V and ±0.075 mA cm^{-2}, respectively. As shown in Fig. 2d, the V_{OC} value of lateral photovoltaic devices connected in series is the sum of each unit cell, whereas the J_{SC} remains almost constant, indicating a uniform performance of each unit cell. A large V_{OC} of 47 V was

observed for devices with 125 unit cells connected in series under illumination of 25 mW cm^{-2}.

To determine the origin of the switchable photovoltaic effect in OTP devices, we examined three possible mechanisms which have been reported for switchable photovoltaic or memristor behaviour, which was also speculated to result in photocurrent hysteresis with a changed photocurrent scanning direction and scanning rate in some perovskite photovoltaic devices[17]: ferroelectricity of the photoactive layer[18]; charge traps in the active layer's surface[17,19]; and motion and accumulation of ions inducing a doping effect[10,20]. Some theoretical calculations have predicted strong ferroelectricity for MAPbI$_3$, with a polarization charge density of the order of 38 C m^{-2} (refs 21,22). However, no ferroelectric polarization was detected from these devices with comparable voltage scanning rates
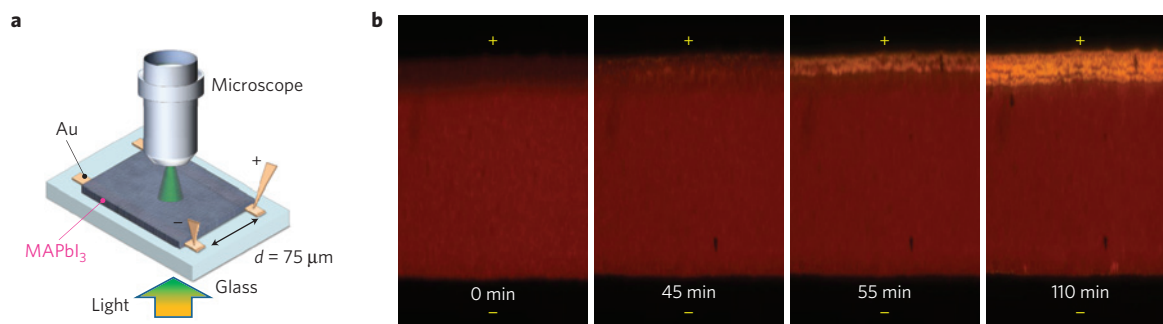
Figure 4 | *In situ* monitoring of the material change during the poling process. a, Illustration of the set-up used for *in situ* monitoring of the poling process using a lateral structure device. **b,** Snapshots of the *in situ* recorded video, showing changed perovskite material close to the anode side during the poling process. The electrical field applied on the perovskite film was ~1.2 V μm^{-1}.

to those in the photovoltaic study when they were measured at both room temperature and 77 K (Supplementary Fig. 10). Piezoresponse force microscopy (PFM) imaging and hysteresis loop measurements showed nothing resembling ferroelectric activity in the MAPbI$_3$ perovskite films—that is, there were weak PFM amplitude and phase signals and no hysteresis switching activity, despite the application of a much higher bias than in the switchable photovoltaic studies. Furthermore, the ferroelectric photovoltaic effect can be excluded by the unchanged photovoltage with respect to the electrode spacing in the lateral structure devices, (Supplementary Fig. 9) and diminished switching behaviour at reduced temperature (Supplementary Fig. 14). Our finding does not, in principle, rule out ferroelectricity in MAPbI$_3$, as more measurements (such as temperature-dependent dielectric and structural testing) are required to clarify this issue. The charge-trapping mechanism can also be excluded because it cannot explain flipping in the direction of the photovoltage and photocurrent, or the persistence of the photocurrent output long after poling, as shown in Supplementary Fig. 11. It was previously reported that similar halide-containing perovskites, such as CsPbCl$_3$ and CsPbBr$_3$, are good halide-ion vacancy conductors at elevated temperatures[23]. We ascribe switchable photovoltaics to ion drift under the electric field in the perovskite layer. Theoretical calculations predicted that negatively charged Pb and MA vacancy (V_{Pb}' and V_{MA}') could result in p-type doping, whereas positively charged I vacancy ($V_I^•$) results in n-type doping in MAPbI$_3$ (refs 24,25), which we verified experimentally in a study of composition-dependent self-doping behaviour in MAPbI$_3$ (ref. 26). In this scenario, the electric field causes the drift of charged $V_I^•$, V_{Pb}' and/or V_{MA}', which have low formation energies in MAPbI$_3$ (refs 24,25), to the area near the electrode and forms a p–i–n structure. Our scenario for the switchable photovoltaics is illustrated in Fig. 3a,b, using vertical structure devices as an example. The positively charged ions or vacancies moved to the Au side during positive poling and accumulated there, leading to n-doping in perovskite on the Au side. Similarly, the remaining negative space charge layer can p-dope the perovskite layer close to PEDOT:PSS, forming a p–i–n homojunction structure. A reverse bias can flip the p–i–n structure to n–i–p by forcing ions or ion vacancies to drift in the opposite direction. The memristive dark- and photocurrent hysteresis can also be explained well by the time-dependent drift of ions under the field[27].

To test this scenario, we first measured the doping-induced band-bending in perovskite close to the top Au electrode after poling in the vertical structure devices by means of Kelvin probe force microscopy (KPFM). The p- or n-doping should induce an increase or reduction of the work function for the perovskite top surface, respectively, as illustrated by the energy diagram in Fig. 3c. The long retention of the diode direction indicates that the poling-induced

changes in composition and work function are stable after poling. Au electrodes could be easily peeled off by Scotch tape to expose the poled perovskite films. Fig. 3d illustrates the films used for the KPFM study, where some unpeeled Au areas were intentionally left as a work function reference. As shown in Fig. 3e,f, the work function of the perovskite films was ~0.22 V lower than that of Au after positive poling, and comparable to that of Au after negative poling—which agrees well with the energy diagram in Fig. 3c and supports the proposed doping mechanism. The surface topography showed no obvious change in the poling areas (Supplementary Fig. 12), thus excluding the effect of topography on the surface potential measurement. The discrepancy of the change in perovskite work function with V_{OC} can be explained by possible surface contamination by residues of Au after peeling and/or by moisture/oxygen, as the KPFM measurement was conducted in air. Finally, semiconductor doping generally causes photoluminescence quench, which was also observed for the p- and n-doped perovskite regions close to both the Au and PEDOT:PSS sides, as shown in Fig. 3g,h.

Another conclusive piece of evidence for the drift of ions during the poling process comes from the observation of composition and morphology changes during poling of a lateral structure device. In this study, the device was intentionally poled for a much longer time (2 h) than was needed for the doping effect, such that the change in perovskite composition/morphology was discernible. The transparency of the perovskite film was monitored *in situ* under an optical microscope, as schematically shown in the measurement set-up in Fig. 4a. The dynamic process was recorded on video using a time-accelerated mode (Supplementary Movie 1), several snapshots of which are shown in Fig. 4b. The perovskite stripe area close to the anode became increasingly transparent, and the morphology in this area was completely different from other areas, with many pinholes appearing (Supplementary Fig. 13), indicating the drift of ions from the anode side. The loss of perovskite material on the anode side indicated that the drifting ions were V_{Pb}' and/or V_{MA}'.

The extensive study of the dynamic poling process for devices under varying electric field, temperature, and perovskite film morphology gave support to a mechanism of field-driven ion drift as being responsible for the photovoltaic switching, as shown in Supplementary Fig. 14. Here, a train of voltage pulses with a duration of 0.95 s was applied to the devices and J_{SC} was recorded after each pulse. An elevated temperature and/or applied electric field (by changing either the applied bias or perovskite film thickness) accelerated the poling process (Supplementary Fig. 14a,b), whereas poling was almost frozen at temperatures below 0 °C (Supplementary Fig. 14c). The extent of the photovoltaic switching effect was influenced by the morphology, stoichiometry and film quality of the perovskite films owing to their influence on the defect concentration. For example, poling became more

difficult (Supplementary Fig. 14d–f) in a device with a much larger perovskite grain size which was formed by a solvent-annealing process. This can be explained by the reduced vacancy concentration in solvent-annealed perovskite films due to fewer grain boundaries resulting from the solvent-annealing process increasing the grain size from 300 nm to range 600–1,000 nm (ref. 28). The statistics of device performance during the dynamic poling process under different measurement conditions and with different film morphologies are shown in Supplementary Fig. 14g. These results confirmed that the switchable photovoltaic behaviour of the devices is due to ion drift.

The best device parameters in the single-layer vertical structure devices after poling approached those of optimized multi-layer devices with both electron- and hole-transporting layers. This work indicates a new direction for perovskite solar cell design using the controlled doping of perovskite for homojunction solar cells, thus reducing device fabrication complexity. The lateral structure device is particularly interesting because it eliminates the need for transparent electrodes, but its efficiency is still limited by the charge carrier diffusion length in present perovskite materials. Further improvements in crystal quality and surface passivation techniques will help to resolve this issue. The perovskite memristors reported here can be read out not only by electrical pulses but also by optical pulses[18]. This work paves the way towards a new approach to doping perovskite using electric pulses, such that a doping pattern can be programmed and directly written using scanning probe microscopy for memristor array fabrication. This might open up new applications for perovskite materials in optoelectronic computational devices, as memristors are being increasingly pursued for computing[29,30].

Methods

CH_3NH_3I precursor synthesis. Methylammonium iodide (CH_3NH_3I) was synthesized using a previously described method[1]. A concentrated aqueous solution of hydroiodic acid (HI) (15.0 ml, 57 wt% in water, Alfa Aesar) was reacted with methylamine (CH_3NH_2) (13.5 ml, 40 wt% in aqueous solution, Alfa Aesar) at 0 °C for 2 h with constant stirring under a nitrogen atmosphere. Methylammonium iodide was crystallized by removing the solvent using a rotary evaporator. The white powder produced was washed with diethyl ether (Alfa Aesar) three times and dried in vacuum overnight.

Film formation and device fabrication. Poly(3,4-ethylenedioxythiophene):poly(4-styrenesulphonate) (PEDOT:PSS) (Baytron-P 4083) was spin-coated on clean indium tin oxide (ITO) substrates at a speed of 3,000 revolutions per minute (r.p.m.). The films were then annealed at 105 °C for 30 min. PbI_2 and MAI were first dissolved in dimethylformamide (DMF) and 2-propanol, respectively. The $MAPbI_3$ films were formed by spin coating PbI_2 (400 mg ml^{-1} in DMF) and (45 mg ml^{-1} in 2-propanol) sequentially at 6,000 r.p.m. for 35 s, respectively, followed by thermal annealing at 100 °C for 2 h. The $MAPbI_{3-x}Cl_x$ films were formed by spin coating PbI_2 (400 mg ml^{-1} in DMF) and $MAI_{0.8}Cl_{0.2}$ (45 mg ml^{-1} in 2-propanol) sequentially at 6,000 r.p.m. for 35 s, respectively, followed by thermal annealing at 110 °C for 1 h. The $FAPbI_3$ films were formed by spin coating PbI_2 (400 mg ml^{-1} in DMF) and FAI (45 mg ml^{-1} in 2-propanol) sequentially at 6,000 r.p.m. for 35 s, respectively, followed by thermal annealing at 120 °C for 1 h. The $MAPbBr_3$ films were formed by spin coating $PbBr_2$ (600 mg ml^{-1} in DMF) and MABr (65 mg ml^{-1} in 2-propanol) sequentially at 6,000 r.p.m. for 35 s, respectively, followed by thermal annealing at 100 °C for 1 h. After spin coating the above inorganic materials, the films were dried at 70 °C for 30 min before spin coating the organic component. For the solvent annealing of perovskite films, approximately 10 μl DMF was introduced into the Petri dishes during the thermal-annealing process. The devices were completed by the thermal evaporation of 50 nm gold (Au) as an electrode.

For lateral photovoltaic devices, the Au stripe arrays were first fabricated on glass substrates by photolithography—that is, the 50 nm thick Au layer was thermally deposited on a pre-patterned photoresist layer, then the photoresist was removed by acetone. The positive photoresistor, Shipley S-1813, was used. The resulting Au stripe patterns have lengths of 3 mm, and spacings of 8 μm (Fig. 2b). The total width of lateral photovoltaic devices connected in series comprising 125 cells is ~1.4 mm. Perovskite films were then fabricated on these substrates using the same method as for vertical device fabrication. The resulting structure of the lateral devices is shown schematically in Fig. 2a. The thickness of the perovskite films for both vertical and lateral device structures is 300 nm, except where specifically labelled.

Film and device characterization. The steady-state photocurrent curves were measured under simulated AM 1.5G irradiation (100 mW cm^{-2}) using a Xenon-lamp-based solar simulator (Oriel 67005, 150 W Solar Simulator). A Schott visible-colour glass-filtered (KG5 colour-filtered) Si diode (Hamamatsu S1133) was used to calibrate the light intensity before photocurrent measurements. A Keithley 4200 semiconductor analyser was used to apply a scanning bias and test the output current simultaneously. All the electrical tests for vertical devices were conducted in a glovebox. Lateral solar cell measurements were conducted in a probe station chamber under a vacuum of 10^{-3} Torr, wherein light (25 mW cm^{-2}) was incident through a quartz window. A Keithley 240a High Voltage Supply with a maximum voltage output of 1,200 V was used for the poling process. The electrical field applied on the perovskite film is ~1.2 V μm^{-1} for 100 s. The poling of the cells was conducted either by poling each cell individually or by simply poling the whole area between the first and last electrodes. For lateral devices, the poling bias lasted for ~100 s, a period longer than in the vertical devices, owing to the much greater ion drift distance. After poling, the $I–V$ curves were measured using a Keithley 2400.

Observation of the *in situ* poling process under a microscope. *In situ* observation of the ion drift under an electric field was carried out by locating the samples under an optical microscope (Olympus BX61) coupled to a high-resolution charge-coupled device (CCD) camera (Photometrics, CoolSNAP-cf). The optical microscope worked in the transmission mode with the sample illuminated from bottom. The samples were kept in a steady N_2 flow during the poling process to prevent the absorption of oxygen and moisture.

KPFM, PFM and atomic force microscopy (AFM). KPFM and AFM measurements were carried out with a Dimension Icon (Bruker) in air and in the dark. Platinum–iridium-coated conductive probes (SCM-PIT, Bruker) were used in the KPFM and AFM measurements. The PeakForce KPFM mode, combining the tapping mode AFM with frequency modulation KPFM can measure the topographic and surface potential signals of the same area. The scanning area and tip velocity were 20 μm × 20 μm and 81.4 μm s^{-1}, respectively. The lift height for KPFM measurements was 80 nm for all samples. PFM was performed by applying a high-frequency modulation voltage (200–600 kHz, 1.0–1.5 V) to the Pt–Ti-coated silicon (Mikromasch) or Au-coated SiN tips (Olympus). Local piezoelectric hysteresis loops were measured in fixed locations on the film as a function of a d.c. bias superimposed on the a.c. modulation voltage.

For sample preparation, the vertical structure devices were first poled in a glovebox. Subsequently, most areas of the top gold electrodes were peeled off by Scotch tape, but some small areas of the Au electrode were purposely left as the reference for the KPFM surface work function.

Ferroelectricity characterization. The ferroelectric polarization measurements were carried out using a Precision Premier II from Radiant Technologies, both at room temperature and 77 K, (by soaking the samples in liquid nitrogen for 10 min before the measurements). The voltage scanning rate applied was 0.08 V s^{-1}, which is comparable to or slower than the rate of photocurrent scanning for the switchable photovoltaic effect study. The data was collected using the software package 'Vision' which is integrated in the Precision Premier II.

References

1. Lee, M. M. *et al.* Efficient hybrid solar cells based on meso-superstructured organometal halide perovskites. *Science* **338,** 643–647 (2012).
2. Burschka, J. *et al.* Sequential deposition as a route to high-performance perovskite-sensitized solar cells. *Nature* **499,** 316–319 (2013).
3. Liu, M., Johnston, M. B. & Snaith, H. J. Efficient planar heterojunction perovskite solar cells by vapour deposition. *Nature* **501,** 395–398 (2013).
4. Liu, D. & Kelly, T. L. Perovskite solar cells with a planar heterojunction structure prepared using room-temperature solution processing techniques. *Nature Photon.* **8,** 133–138 (2013).
5. Heo, J. H. *et al.* Efficient inorganic–organic hybrid heterojunction solar cells containing perovskite compound and polymeric hole conductors. *Nature Photon.* **7,** 486–491 (2013).
6. Edri, E. *et al.* Elucidating the charge carrier separation and working mechanism of $CH_3NH_3PbI_3-xCl_x$ perovskite solar cells. *Nature Commun.* **5,** 3461 (2014).
7. Kojima, A., Teshima, K., Shirai, Y. & Miyasaka, T. Organometal halide perovskites as visible-light sensitizers for photovoltaic cells. *J. Am. Chem. Soc.* **131,** 6050–6051 (2009).

197

8. Im, J-H. *et al.* 6.5% efficient perovskite quantum-dot-sensitized solar cell. *Nanoscale* **3,** 4088–4093 (2011).

9. Kim, H-S. *et al.* Lead iodide perovskite sensitized all-solid-state submicron thin film mesoscopic solar cell with efficiency exceeding 9%. *Sci. Rep.* **2,** 591 (2012).

10. Choi, T. *et al.* Switchable ferroelectric diode and photovoltaic effect in BiFeO$_3$. *Science* **324,** 63–66 (2009).

11. Grinberg, I. *et al.* Perovskite oxides for visible-light-absorbing ferroelectric and photovoltaic materials. *Nature* **503,** 509–512 (2013).

12. Xiao, Z. *et al.* Efficient, high yield perovskite photovoltaic devices grown by interdiffusion of solution-processed precursor stacking layers. *Energy Environ. Sci.* **7,** 2619–2623 (2014).

13. Chen, Q. *et al.* Planar heterojunction perovskite solar cells via vapor assisted solution process. *J. Am. Chem. Soc.* **136,** 622–625 (2013).

14. Yuan, Y., Xiao, Z., Yang, B. & Huang, J. Arising applications of ferroelectric materials in photovoltaic devices. *J. Mater. Chem. A* **2,** 6027–6041 (2014).

15. Stranks, S. D. *et al.* Electron–hole diffusion lengths exceeding 1 micrometer in an organometal trihalide perovskite absorber. *Science* **342,** 341–344 (2013).

16. Xing, G. *et al.* Long-range balanced electron- and hole-transport lengths in organic–inorganic CH$_3$NH$_3$PbI$_3$. *Science* **342,** 344–347 (2013).

17. Snaith, H. J. *et al.* Anomalous hysteresis in perovskite solar cells. *J. Phys. Chem. Lett.* **5,** 1511–1515 (2014).

18. Guo, R. *et al.* Non-volatile memory based on the ferroelectric photovoltaic effect. *Nature Commun.* **4,** 1990 (2013).

19. Andersson, P., Robinson, N. D. & Berggren, M. Switchable charge traps in polymer diodes. *Adv. Mater.* **17,** 1798–1803 (2005).

20. Yi, H. *et al.* Mechanism of the switchable photovoltaic effect in ferroelectric BiFeO$_3$. *Adv. Mater.* **23,** 3403–3407 (2011).

21. Frost, J. M. *et al.* Atomistic origins of high-performance in hybrid halide perovskite solar cells. *Nano Lett.* **14,** 2584–2590 (2014).

22. Stoumpos, C. C., Malliakas, C. D. & Kanatzidis, M. G. Semiconducting tin and lead iodide perovskites with organic cations: Phase transitions, high mobilities, and near-infrared photoluminescent properties. *Inorg. Chem.* **52,** 9019–9038 (2013).

23. Mizusaki, J., Arai, K. & Fueki, K. Ion-conduction of the Perovskite-type Halides. *Solid State Ion.* **11,** 203–211 (1983).

24. Yin, W-J., Shi, T. & Yan, Y. Unusual defect physics in CH$_3$NH$_3$PbI$_3$ perovskite solar cell absorber. *Appl. Phys. Lett.* **104,** 063903 (2014).

25. Kim, J., Lee, S-H., Lee, J. H. & Hong, K-H. The role of intrinsic defects in methylammonium lead iodide perovskite. *J. Phys. Chem. Lett.* **5,** 1312–1317 (2014).

26. Wang, Q. *et al.* Qualifying composition dependent p and n self-doping in CH$_3$NH$_3$PbI$_3$. *Appl. Phys. Lett.* **105,** 163508 (2014).

27. Yang, J. J. *et al.* Memristive switching mechanism for metal/oxide/metal nanodevices. *Nature Nanotech.* **3,** 429–433 (2008).

28. Xiao, Z. *et al.* Solvent-annealing of perovskite induced crystal growth for photovoltaic device efficiency enhancement. *Adv. Mater.* **26,** 6503–6509 (2014).

29. Yang, J. J., Strukov, D. B. & Stewart, D. R. Memristive devices for computing. *Nature Nanotech.* **8,** 13–24 (2013).

30. Borghetti, J. *et al.* 'Memristive' switches enable 'stateful' logic operations via material implication. *Nature* **464,** 873–876 (2010).

Author contributions

J.H. conceived and supervised the project. Z.X. fabricated and measured the vertical structure device. Y.Y. and Q.W. fabricated and measured the lateral structure device. Y.S. conducted the KPFM measurement. Q.D. synthesized the MAI material. P.S. and A.G. conducted the PFM measurement. All authors analysed the data and wrote the manuscript.

Additional information

Supplementary information is available in the online version of the paper. Reprints and permissions information is available online at www.nature.com/reprints. Correspondence and requests for materials should be addressed to J.H.

Competing financial interests

The authors declare no competing financial interests.

Giant switchable photovoltaic effect in organometal trihalide perovskite devices

Zhengguo Xiao, Yongbo Yuan, Yuchuan Shao, Qi Wang, Qingfeng Dong, Cheng Bi, Pankaj Sharma, Alexei Gruverman and Jinsong Huang

In the version of this Letter originally published online, the (′) and (·) symbols where reversed. In keeping with the Kröger–Vink notation, the (′) should indicate a negative charge and (·) a positive charge, thus the following sentences should have read "Theoretical calculations predicted that negatively charged Pb and MA vacancy ($V_{Pb}′$ and $V_{MA}′$) could result in p-type doping, whereas positively charged I vacancy ($V_I·$) results in…", "In this scenario, the electric field causes the drift of charged $V_I·$, $V_{Pb}′$ and/or $V_{MA}′$, which have low formation energies…" and "The loss of perovskite material on the anode side indicated that the drifting ions were $V_{Pb}′$ and/or $V_{MA}′$." These errors have now been corrected in all versions of the Letter.